sustainability

MDPI

Article

Transition Dynamics of Geological Disaster Resilience and Network Structure Analysis in Mountain Cities: Evidence from County-Level Areas in Western Sichuan Province, China

Kang Meng [1], Yusen Lin [1] and Hao Yin [1,2,*]

[1] School of Architecture and Civil Engineering, Xihua University, Chengdu 610039, China; mengkang@mail.xhu.edu.cn (K.M.); 212024085900025@stu.xhu.edu.cn (Y.L.)
[2] Department of Construction Management, Dalian University of Technology, Dalian 116024, China
* Correspondence: yinhao1011@mail.dlut.edu.cn

Abstract

Against the background of intensifying global climate change and the continued expansion of human activities into mountainous areas, geological hazards such as landslides, rockfalls, and debris flows have become increasingly frequent, posing serious challenges to urban safety and sustainable development in mountainous regions. From a resilience perspective, this study selects 19 cities in western Sichuan Province as the study area and develops a three-dimensional geological-hazard resilience framework comprising adaptation, resistance, and recovery capacities. The entropy weight–TOPSIS method is employed to assess geological-hazard resilience from 2018 to 2022, while kernel density estimation, Markov chains, an improved gravity model, and social network analysis are integrated to investigate spatiotemporal evolution and network structure. The results show that: (1) geological-hazard resilience generally increased across the study area, while regional disparities continued to widen; (2) the three resilience dimensions gradually shifted from imbalance toward greater coordination, with adaptation and recovery capacities improving markedly, whereas resistance capacity remained relatively weak and exhibited greater fluctuations; (3) temporally, the kernel density distribution evolved from a sharper to a flatter pattern, indicating some improvement among low-resilience areas while differentiation persisted; spatially, resilience exhibited an "east-high, west-low" pattern, together with evident path dependence and neighborhood effects. Low-resilience areas showed relatively high state persistence, and upward transition probabilities varied under different neighborhood conditions; and (4) the spatial network structure became progressively denser, with increasing intercity connections and network density, although diffusion toward western areas remained limited and regional development disparities persisted. These findings provide a basis for disaster risk reduction and coordinated regional resilience governance in mountainous cities. This study provides theoretical support and decision-making references for disaster prevention and mitigation as well as regional coordinated governance in mountainous cities.

Keywords: mountainous cities; geo-disaster resilience; Markov chain; social network analysis

Check for updates

Academic Editor: Fernando Fonseca

Received: 18 September 2026
Revised: 25 October 2026
Accepted: 27 October 2026
Published: 29 October 2026

Copyright: © 2026 by the authors. Licensee MDPI, Basel, Switzerland. This article is an open access article distributed under the terms and conditions of the Creative Commons Attribution (CC BY) license.

1. Introduction

Against the backdrop of ongoing global climate change, intensified precipitation, uneven spatiotemporal distribution, and the increasing frequency of extreme events have significantly amplified the uncertainty of natural systems and continuously exacerbated

geo-disaster risks [1]. Compared with plain regions, mountainous cities—characterized by complex topography and fragile ecological systems—are more sensitive to climatic anomalies. These conditions tend to trigger landslides, collapses, and debris flows, along with cascading disaster effects, thereby imposing stronger constraints on urban safety and sustainable development [2–4].

China, with its vast territory and highly diverse geomorphological and climatic conditions, is one of the countries with the most pronounced natural geographical heterogeneity in the world, and it also reports one of the highest numbers of natural disaster events [5]. Although China's comprehensive capacity for geo-disaster prevention and control has improved significantly in recent years, leading to a general reduction in overall risk levels, interannual fluctuations and structural risks remain prominent. Given the inevitability of geo-disasters, human societies must learn to "coexist with hazards," and enhancing resilience has become a key strategy for disaster mitigation. The United Nations Office for Disaster Risk Reduction has emphasized that strengthening disaster resilience contributes to sustainable development and vulnerability reduction, warranting further in-depth research [6]. In this context, systematically assessing the adaptation, resistance, and recovery capacities of mountainous cities under disaster disturbances from a resilience perspective has become an important shift in disaster risk reduction research.

To review the research progress in the field of geological disasters, this study conducted keyword co-occurrence and cluster analyses using CiteSpace, based on 5483 SCI/SSCI publications indexed in the Web of Science database from 2016 to 2025. As shown in Figure 1, the results indicate that existing research has primarily focused on surface deformation monitoring, landslide and debris flow susceptibility assessment, disaster prediction, and risk assessment, with increasing attention being paid to the impacts of climate change and associated environmental processes on geological disasters [7–24]. These studies have provided an important foundation for geological hazard identification and risk assessment. Meanwhile, extending the research focus from disaster risk assessment to the adaptive, resistance, and recovery capacities of regional systems under disaster disturbances has become an important direction in disaster resilience research. Compared with studies primarily concerned with the spatial distribution of hazards and the conditions contributing to disaster occurrence, geological disaster resilience assessment places greater emphasis on the comprehensive response capacities of regional systems and their dynamic changes, thereby providing a complementary perspective for understanding the relationship between disaster risk and regional development in mountainous counties [25–29].

In recent years, related studies have made continuous progress in both indicator system construction and methodological applications. For example, Huang et al. [30] developed a multidimensional indicator system from environmental and social resilience perspectives and combined random forest with the AHP-TOPSIS method to quantitatively assess geo-disaster resilience in mountainous cities, revealing significant spatial clustering patterns. Wang et al. [31] constructed a "threat–resilience–damage" analytical framework based on a modified community baseline resilience index and applied a coupling coordination model to analyze inter-county system interactions and their impacts on disaster losses. Building on these advances, Zhu et al. [32] further integrated SBM-DEA, spatial Markov chains, the GeoDetector model, and geographically and temporally weighted regression (GTWR) to deepen the understanding of geo-disaster resilience from both spatiotemporal evolution and driving mechanism perspectives.

Compared with studies that characterize regional resilience primarily through composite indicators, another strand of research places greater emphasis on the temporal dynamics of resilience, viewing resilience as a continuous process in which systems experience performance degradation, resistance, recovery, and subsequent readjustment under

disaster disturbances. Early resilience research regarded the ability of a system to withstand disturbances and restore functionality as a core component of resilience, emphasizing characteristics such as robustness, redundancy, resource mobilization capacity, and recovery speed. Subsequent studies further argued that resilience assessment should consider not only the state of a system at a particular point in time, but also the temporal evolution of system performance before and after disturbances. The review by Hosseini et al. on system resilience showed that absorptive, adaptive, and recovery capacities are common components of most resilience definitions. More recent studies have further considered recurrent hazards and the repeated processes of performance degradation and recovery that they may induce [33]. Wei et al. developed system availability and resilience assessment models for recurrent and interdependent hazards and incorporated restoration decisions into resilience optimization to characterize repeated failure–recovery processes under recurrent disturbances. Their findings indicate that, when hazards are recurrent and dependent, static assessments based on a single disturbance may be insufficient to fully characterize system resilience [34]. Building on this work, Wei et al. further extended the analysis to engineered networks composed of nodes and links, considering multimodal system performance changes caused by multiple recurrent hazards and overlapping hazard impacts. Network robustness and recoverability were evaluated from both performance level and rate-of-change perspectives, while critical nodes and links were also identified [35]. Collectively, these studies demonstrate that resilience is characterized by pronounced temporal dependence and network interdependence, and that the understanding of resilience is gradually extending from single-time-point capacity assessment toward dynamic processes involving disturbance, performance change, recovery, and network-structure evolution.

However, existing studies of dynamic resilience have largely focused on engineered systems or infrastructure networks with clearly defined physical functions and continuous performance metrics. Such analyses generally rely on event-scale information, including hazard occurrence times, component failure states, functional losses, and recovery durations. For mountainous counties, which represent complex territorial systems jointly shaped by social, economic, infrastructural, and hazard-related conditions, such high-temporal-resolution performance data are often difficult to obtain. Consequently, regional resilience studies still rely primarily on annual or stage-based composite capacity indicators. Therefore, without equating annual composite resilience indicators with event-based engineering performance recovery trajectories, there remains a need to further investigate intertemporal changes in regional resilience states, the persistence and transition of resilience levels, and potential spatial association structures among counties.

Overall, existing geological-hazard resilience research has made considerable progress in indicator-system development and the identification of spatial disparities, yet two issues warrant further investigation. First, county-level studies still tend to focus on resilience levels and their spatial differentiation at a particular time or across several discrete time points, while comparatively limited attention has been paid to the persistence, improvement, or deterioration of resilience states over consecutive years. This limits the understanding of the dynamic evolution of regional resilience from the perspective of state transitions. Second, although recent dynamic resilience studies have increasingly considered recurrent disturbances and changes in network performance, they have mainly focused on engineered systems characterized by explicit nodes, links, and functional performance trajectories. For mountainous county systems composed of interacting social, economic, and infrastructural components, the relationship between changes in resilience states and regional spatial association structures remains insufficiently examined. It is therefore necessary, while maintaining a clear conceptual distinction between regional composite resilience assessment and event-scale resilience modeling of engineered systems, to examine the dynamic evolution of

geological-hazard resilience in mountainous counties from three interconnected dimensions: resilience level, state transition, and spatial association networks.

Accordingly, this study focuses on 19 mountainous counties (county-level cities) in western Sichuan Province and develops a three-dimensional geological-hazard resilience assessment framework comprising adaptation, resistance, and recovery capacities. The analysis proceeds through three interconnected levels. First, the entropy weight–TOPSIS method is used to quantify county-level geological-hazard resilience from 2018 to 2022, and kernel density estimation (KDE) is employed to characterize changes in its overall distribution. Second, conventional Markov chains and spatial Markov chains are used to examine the intertemporal persistence and transition of different resilience states, as well as differences in transition probabilities under different neighborhood conditions. Finally, a gravity model is used to construct potential resilience association networks among counties, and social network analysis is applied to characterize changes in network structure and nodal positions. Compared with purely static resilience ranking, this study integrates annual changes in resilience states and regional spatial association structures within a unified analytical framework, thereby providing complementary evidence for understanding the longer-term evolution of resilience and coordinated regional governance in mountainous counties.



Figure 1. Network Map of Key Geohazard Keywords in the English Literature.

2. Materials and Methods

2.1. Study Area

The study area covers 19 mountainous counties (cities) in Ya'an City, Ganzi Tibetan Autonomous Prefecture, and Aba Tibetan and Qiang Autonomous Prefecture in western Sichuan Province, as shown in Figure 2. This region is highly representative of mountainous areas along the eastern margin of the Qinghai–Tibet Plateau in China in terms of its geographical environment, disaster types, and socio-economic characteristics, as presented

in Table 1. According to statistics from China's Ministry of Emergency Management, the number of disaster occurrences in this region accounts for approximately 70% of the total in the three prefectures (cities), indicating a high frequency and diversity of natural hazards. These disasters not only pose severe threats to the safety of lives and property but also impose long-term constraints on regional economic structure and sustainable development. Therefore, conducting research on disaster risk and resilience in such typical mountainous areas is both of practical urgency and strongly representative.

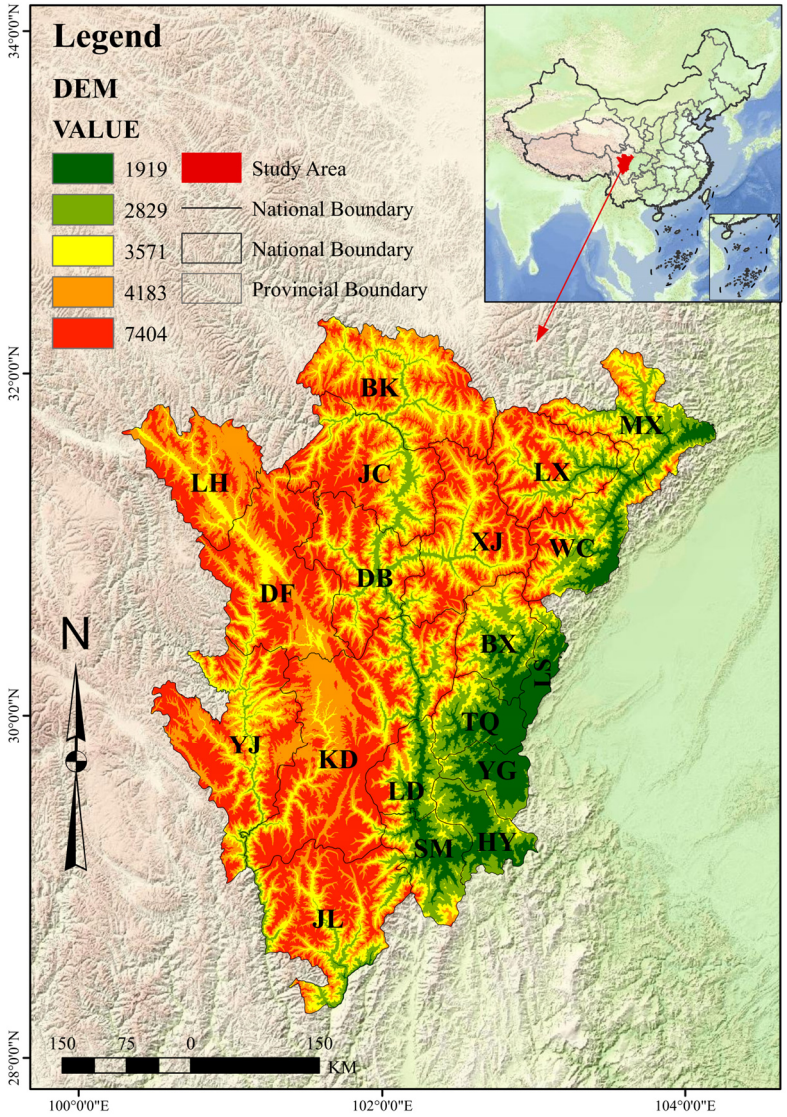

Figure 2. Study Area.

Table 1. Distribution of major landforms and tectonic units in the study area.

Location	Main Landforms	Structural Unit
DB	Deep gorges cut through the high mountains, with pronounced undulations	Longmen Shan Fault Zone
JC	The gorge gives way to a wider valley, opening up in places	Songpan-Ganzi Orogenic Belt
XJ	High mountains and deep valleys, with significant elevation differences	Songpan-Ganzi Orogenic Belt

Table 1. *Cont.*

Location	Main Landforms	Structural Unit
WC	The terrain is rugged, with steep slopes and narrow valleys	Longmen Shan Fault Zone
LX	High mountains and deep gorges, with glacial remnants	Songpan-Ganzi Orogenic Belt
MX	High mountains and deep gorges, with steep slopes and well-defined ravines	Minshan Tectonic Belt
LD	Deep gorges, with severe erosion and steep, deep slopes	Hengduan Mountain Orogenic Belt
SM	The gorge is long and narrow, with distinct undulations	Anning River Tectonic Belt
HY	A landscape of alternating gorges and basins, with significant variations in elevation	Hengduan Mountain Orogenic Belt
KD	Transition from highlands to mountains, with a marked gradient	The transitional zone on the eastern edge of the Qinghai–Tibet Plateau
YJ	Mountainous gorges, deep valleys and towering peaks	Songpan-Ganzi Orogenic Belt
JL	High mountains and deep gorges, with a dense network of ravines and dramatic undulations	Hengduan Mountain Orogenic Belt
DF	Mountainous and valley regions, distributed in bands	Xianshuihe Fault Zone
LH	Mountainous terrain with wide valleys and some open areas	Xianshuihe Fault Zone
BK	Highland terrain, with gentle undulations and wide valleys	Songpan-Ganzi Orogenic Belt
BX	Mountainous gorges, with deep valleys and steep slopes, and a rugged terrain	Longmen Shan Fault Zone
TQ	Mountainous gorges, with steep slopes, narrow valleys and dramatic undulations	Longmen Shan Fault Zone
LS	The terrain is rugged, with pronounced undulations	Longmen Shan Fault Zone
YG	Low- to medium-altitude mountain valleys with gentle slopes	Longmen Shan Fault Zone

2.2. Method

Taking 19 mountainous cities in western Sichuan Province as the research objects, this study focuses on resilience framework construction, spatiotemporal evolution analysis, and network structure characteristics, and is conducted as follows:

(1) Based on the principles for selecting urban resilience indicators and the constructed analytical framework, and through a comprehensive review of the existing literature, 28 indicators are selected to establish a three-stage geo-disaster resilience framework encompassing adaptation, resistance, and recovery.
(2) The entropy-weighted TOPSIS method is applied to calculate the geo-disaster resilience index of the study area from 2018 to 2022, and to analyze the overall resilience levels of cities as well as differences in their stage-specific capacities.
(3) From a temporal perspective, kernel density estimation is employed to examine the evolutionary trends of geo-disaster resilience and the changing characteristics of the three-stage capacities (adaptation–resistance–recovery), thereby revealing their structural features; from a spatial perspective, the Markov chain method is introduced to explore transition pathways and transfer characteristics among different resilience levels.
(4) An improved gravity model is used to quantitatively measure the strength of interregional resilience linkages, which are then transformed into a binary gravity matrix and

incorporated into social network analysis to identify network structure characteristics and differences in node types.

2.2.1. Entropy Weighted Method—TOPSIS Method

The entropy weight method is employed to objectively assign weights to each evaluation indicator. This method is based on the degree of dispersion of indicator data, using information entropy to characterize the uncertainty of information and applying the coefficient of variation to determine weights, thereby reflecting the contribution of each indicator in the comprehensive evaluation. Compared with subjective weighting methods, the entropy weight method can, to a certain extent, reduce the influence of human factors; however, its results are still affected by the distribution characteristics of the data.

The entropy weights are then incorporated into the TOPSIS model. The standardized indicator matrix is weighted, and the relative closeness is calculated by measuring the distances between each evaluation unit and the positive and negative ideal solutions, which is used to represent the regional resilience level.

Since the constructed evaluation indicator system includes both positive and negative indicators, differences exist among indicators in terms of numerical meaning, direction of change, and measurement scale. To eliminate the influence of dimensionality and unify the direction of variation across indicators, normalization is performed. For positive indicators, where larger values indicate higher evaluation levels, Equation (2) is used for normalization; for negative indicators, where larger values indicate lower evaluation levels, Equation (3) is applied accordingly. After normalization, the standardized evaluation matrix Z is obtained

$$X_t = \left[xi_{qt} \right]_{N \times Q} \tag{1}$$

xi_{qt}: the raw value of indicator q for city i in year t;
N: the number of cities;
Q the number of indicators.
Standardized:

$$Z_{iq} = \frac{r_{iq} - min(r_{iq})}{max(x_{iq}) - min(x_{iq})} \tag{2}$$

$$Z_{iq} = \frac{max(x_{iq}) - r_{iq}}{max(x_{iq}) - min(x_{iq})} \tag{3}$$

$$Z = \left[z_{iq} \right]_{N \times Q} \tag{4}$$

In the formula, Z denotes the standardized evaluation matrix. Z_{ij} represents the standardized value of indicator j for city i, where $i = 1, 2, \ldots,$ n and n is the number of evaluation units, and $q = 1, 2, \ldots,$ m and m is the number of evaluation indicators.

$$P_{iq} = \frac{z_{iq}}{\sum_{i=1}^{N} z_{iq}} \tag{5}$$

Here, P_{iq} represents the proportion of the value of indicator j for city i relative to the total value of that indicator.

$$e_q = -\frac{\sum_{i=1}^{N} p_{iq} \ln p_{iq}}{\ln n} \tag{6}$$

The information entropy e_q of indicator j is used to characterize the uncertainty and dispersion of the indicator information, where n in $\ln n$ denotes the number of evaluation units.

$$g_q = 1 - e_q \tag{7}$$

The coefficient of variation e_q reflects the amount of effective information contained in the indicator.

$$w_q = \frac{g_q}{\sum_{q=1}^{Q} g_q} \tag{8}$$

$$v_{iq} = w_q \times z_{iq} \tag{9}$$

Compute the weight w_q of each indicator according to Equation (8), and apply these weights to the standardized matrix Z using Equation (9).

For the quantification of the geological disaster resilience index, calculations are carried out using the TOPSIS method based on the weighted standardized evaluation matrix obtained in Step.

$$v_q^+ = \max_i v_{iq} \tag{10}$$

The optimal state v_q^+ is determined by the positive ideal solution, representing an ideal condition in which all evaluation indicators reach their optimal levels.

$$v_q^- = \min_i v_{iq} \tag{11}$$

The worst state v_q^- is determined by the negative ideal solution, representing an ideal condition in which all evaluation indicators are at their lowest levels.

$$D_i^+ = \sqrt{\sum_{q=1}^{Q} \left(v_{iq} - v_q^+\right)^2} \tag{12}$$

The distance D_i^+ between the i-th city and the positive ideal solution.

$$D_i^- = \sqrt{\sum_{q=1}^{Q} \left(v_{iq} - v_q^-\right)^2} \tag{13}$$

The distance D_i^- between the i-th city and the negative ideal solution.

$$GRI_i = \frac{D_I^-}{D_i^+ + D_i^-} \tag{14}$$

In the equation, i denotes a mountainous city within the study area. A larger GRI_i value indicates a higher level of geological disaster resilience, whereas a smaller GRI_i value signifies a relatively lower level of resilience.

2.2.2. Kernel Density Estimation (KDE)

Kernel density estimation (KDE) is used to characterize the distribution features and evolutionary process of the geological disaster resilience index across different periods. By applying non-parametric smoothing to spatial unit samples, it avoids the information loss caused by arbitrary classification.

$$f(R) = \frac{1}{nh} \sum_{i=1}^{n_t} K\left(\frac{GRI - GRI_i}{h}\right) \tag{15}$$

$$K(u) = \frac{1}{\sqrt{2\pi}} e^{-\frac{1}{2}u^2} \tag{16}$$

In the equation, $f(R)$ denotes the estimated density function value at a given GRI value; n is the sample size; x_i represents the value of the i-th observation; K is the Gaussian kernel function; and h is the bandwidth parameter.

2.2.3. Markov Chain

(1) Traditional Markov chain

A Markov chain is a method used to describe the stochastic process of system state transitions over time. Its core characteristic is the Markov property (memory lessness), meaning that given the current state, the future state of the system depends only on the present state and is independent of past states.

$$S_{i,t} \in \{1, 2, \ldots., K\}$$

$$P\left(S_{i,t+1} = s | S_{i,t} = r, S_{i,t-1}, \ldots\right) = P\left(S_{i,t+1} = s | S_{i,t} = r\right) \tag{17}$$

$$P = \begin{bmatrix} p_{11} & p_{12} & \cdots & p_{1K} \\ p_{21} & p_{22} & \cdots & p_{2K} \\ \vdots & \vdots & \ddots & \vdots \\ p_{K1} & p_{K2} & \cdots & p_{KK} \end{bmatrix} \tag{18}$$

$$P_{rs} = P\left(S_{i,t+1} = s | S_{i,t} = r\right) = \frac{n_{rs}}{\sum_{s=1}^{K} n_{rs}} \tag{19}$$

S: the subsequent state;

n_{rs}: the observed number of transitions from state r to state s;

K: denotes the number of resilience states.

(2) Spatial Markov chain

The traditional Markov chain ignores spatial dependence and assumes that spatial units are mutually independent. However, in geological disaster resilience and urban systems, there are significant spatial spillover effects among units. Therefore, it is necessary to introduce spatial lag states into the Markov chain—i.e., the spatial Markov chain—to capture the influence of neighborhood conditions on state transitions.

$$w_{ij} = \begin{cases} 1, If\ region\ i\ shares\ a\ boundary\ with\ region\ j. \\ 0, Otherwise. \end{cases} (i \neq j) \tag{20}$$

$$\tilde{W}_{ij} = \frac{w_{ij}}{\sum_{j=1}^{N} W_{ij}}$$

$$L_{i,t} = \sum_{j=1}^{N} \tilde{W}_{ij} GRI_i \tag{21}$$

$C_{i,t} \in \{1, 2, 3\}$;

1 = low-resilience neighborhood;

2 = medium-resilience neighborhood;

3 = high-resilience neighborhood.

$$p_{rs}^{(k)} = P\left(S_{s,t+1} = s | S_{i,t} = r, C_{i,t} = k\right) \tag{22}$$

$$K = 1, 2, 3$$

$$p^{(k)} = \left[p_{rs}^{(K)}\right]_{K \times k} \tag{23}$$

A spatial lag variable is constructed, and a spatial weight matrix is established using the Queen contiguity criterion, as shown in Equation (20). Let the geological disaster resilience of the i-th spatial unit at time t be GRI_i; the spatial lag state can then be defined as in Equation (21). Under the condition of a given spatial lag resilience level k, the transition probability of resilience levels can be calculated using Equation (22), yielding the Markov transition matrices under different neighborhood states, as presented in Equation (23). In the equation, w_{ij} denotes the spatial weight matrix, and $L_{i,t}$ represents the neighborhood resilience level of unit i.

2.2.4. Network Analysis Method

(1) Improved gravity model

Based on the spatial association of resilience among cities and the characteristics of distance decay, a gravity model is employed to characterize the strength of inter-city linkages. Euclidean distance is used as the impedance factor to calculate the resilience-based gravitational values between cities, which are then used to represent the structure of the urban network.

$$\theta_{ij,t} = \frac{GRI_{i,t}}{GRI_{i,t} + GRI_{j,t}} \tag{24}$$

$\theta_{ij,t}$ is a directional correction coefficient, which introduces directionality into the otherwise symmetric gravity interaction between cities i and j.

$$F_{ij,t} = \theta_{ij} \frac{GRI_{i,t} \times GRI_{j,t}}{d_{ij}^2} \tag{25}$$

$F_{ij,t}$: the potential resilience association strength directed from city i to city j in year t; $GRI_{i,t}, GRI_{j,t}$: the geological-disaster resilience indices of cities i and j, respectively d_{ij}; d_{ij}^2: the spatial distance between cities i and j.

$$a_{ij,t} = \begin{cases} 1, F_{ij,t} > \tau \\ 0, F_{ij,t} \leq \tau \end{cases}$$

where $F_{ij,t}$ denotes the potential resilience association strength directed from city i to City j in year t, and τ denotes the binarization threshold. When $F_{ij,t}$ exceeds the threshold τ, the relationship between cities i and j, is defined as a valid directed link; otherwise, no link is assigned.

(2) Social network analysis (SNA)

Social network analysis (SNA) is an important methodological approach for examining structural relationships among cities. Within this framework, cities are treated as nodes in a network, and their interactions constitute the edges, thereby forming an urban network with complex structural characteristics. In this study, cities are considered as network nodes, and the gravitational effects of geological disaster resilience are treated as the network edges.

$$D_t = \frac{L_t}{N(N-1)} \tag{26}$$

N is the number of nodes (cities); L and is the actual number of links.

$$C_i^{out}(t) = \sum_{j=1, j \neq i}^{N} a_{ij,t} \tag{27}$$

$$C_i^{in}(t) = \sum_{j=1, j \neq i}^{N} a_{ji,t} \tag{28}$$

$C_i^{out}(t)$ denotes the out-degree centrality of city i, and $C_i^{in}(t)$ denotes the in-degree centrality of city i. $a_{ij,t} = 1$ indicates the existence of a relationship from city i to city j, while $a_{ij,t} = 0$ indicates that no such relationship exists.

3. Results

3.1. Indicator Construction and Entropy Weight Results

This study focuses on 19 mountainous counties (county-level cities) in western Sichuan Province, China. Considering the complex geological environment, topographical constraints on infrastructure development, and disparities in socioeconomic conditions across the study area, a geological disaster resilience assessment framework comprising three

dimensions—adaptation capacity, resistance capacity, and recovery capacity—was established. The selection of indicators followed the principles of theoretical relevance, applicability to geological disaster contexts, data availability, and interannual comparability. Based on a review of existing disaster resilience studies and the specific characteristics of mountainous counties, 28 indicators were selected to characterize the socioeconomic conditions, infrastructure support, and potential recovery resources associated with geological disaster resilience. Specifically, adaptation capacity reflects the social and institutional conditions supporting adjustment to disaster disturbances, including demographic structure, social security, and healthcare services. Resistance capacity characterizes the potential infrastructure conditions for withstanding disaster disturbances, while incorporating geological hazard levels as external environmental constraints. Recovery capacity reflects the economic and financial resources potentially available for post-disaster functional restoration and socioeconomic adjustment. The data were primarily obtained from the *China Statistical Yearbook*, local *Statistical Communiqués on National Economic and Social Development*, and publicly available government data for the period 2018–2022. The entropy weight method was employed to determine the data-driven weights of the indicators. The indicator system and corresponding weights are presented in Table 2.

Adaptation capacity encompasses demographic characteristics, social security, and healthcare resources that may influence the ability of mountainous counties to adjust to geological disaster disturbances. Population density reflects the spatial concentration of residents, which is associated with disaster exposure and the spatial allocation of public services and emergency resources [36]. Female proportion and rural population proportion characterize demographic composition and urban–rural differences, respectively. These indicators are included as supplementary measures of social adaptation conditions, considering potential differences in disaster-related needs, resource accessibility, and social support among population groups [37,38]. Population growth rate and urbanization rate reflect demographic dynamics and urban–rural development, which may influence adaptation capacity through changes in population distribution, public service provision, and resource allocation [39,40]. Medical insurance coverage represents the institutional basis of social protection, while the number of healthcare personnel and hospital beds reflects the human resources and service capacity available for emergency medical response [41]. Together, these indicators characterize the potential social and institutional conditions supporting county-level adaptation to geological disasters.

Recovery capacity focuses on the economic resources and development conditions potentially available to support post-disaster functional restoration and socioeconomic adjustment. Per capita disposable income and per capita GDP reflect household economic resources and regional economic development, respectively, providing a potential material basis for livelihood recovery and economic reconstruction. Per capita loan levels characterize access to credit resources, although their implications for recovery capacity depend on the associated debt burden and financing conditions [42]. Local fiscal revenue reflects the financial resources available to local governments for public service restoration and infrastructure reconstruction [36]. Tourism revenue, the number of industrial enterprises above designated size, and the proportion of secondary and tertiary industries characterize the scale and structure of regional economic activities, which may influence the availability and diversity of resources for post-disaster recovery [43]. Per capita fixed asset investment and economic density further represent regional capital investment and the spatial concentration of economic activities. These indicators collectively characterize the potential economic foundations for post-disaster recovery rather than directly measuring actual recovery rates or restoration times.

Resistance capacity primarily reflects the potential support provided by infrastructure systems and the external constraints imposed by geological hazards. Construction capacity represents the regional resource base for engineering construction and infrastructure maintenance, which may support the implementation of geological hazard mitigation measures and infrastructure protection. The road area ratio in built-up areas and road density characterize transportation infrastructure provision and spatial accessibility, respectively, while the length of illuminated roads reflects lighting infrastructure available to support transportation under low-visibility conditions [44,45]. Drainage pipeline density, per capita park green space, water supply pipeline length, and gas penetration rate characterize municipal infrastructure and essential service provision. Drainage facilities and green spaces may contribute to rainfall–runoff regulation, whereas water supply and gas infrastructure support the continuity of basic services [46–48]. Communication capacity represents the infrastructure and service conditions potentially supporting disaster warning dissemination and emergency coordination. Furthermore, considering the complex geological structures, pronounced topographic relief, and spatial variation in geological hazard exposure across western Sichuan, the probability of geological disaster occurrence and geological disaster density were incorporated to characterize the likelihood and spatial concentration of geological hazards, respectively. These indicators represent external hazard constraints within the assessment of resistance capacity, thereby strengthening the applicability of the framework to geological disaster contexts in mountainous regions [49–51].

Table 2. Weights of Geological Disaster Resilience Indicators.

Resilience	Number	Indicators	Unit	Weight
Adaptive	X1	Population density	persons km^{-2}	0.0105
	X2	Female proportion	%	0.0175
	X3	Rural population proportion	%	0.0221
	X4	Proportion of population covered by medical insurance	%	0.0020
	X5	Number of healthcare staff	No.	0.0644
	X6	Population growth rate	%	0.0060
	X7	Urbanisation rate	%	0.0336
	X8	Number of beds in healthcare facilities	No.	0.0396
Recovery	X9	Disposable income per capita	CNY $person^{-1}$	0.0366
	X10	GDP per capita	CNY $person^{-1}$	0.0320
	X11	Loans per capita	CNY $person^{-1}$	0.0073
	X12	Local government revenue	10^4 CNY	0.0505
	X13	Revenue from the tourism industry	10^4 CNY	0.0454
	X14	Industrial enterprises above a certain size	No.	0.0627
	X15	Proportion of the secondary and tertiary sectors	%	0.0068
	X16	Per capita investment in fixed assets	CNY·$person^{-1}$	0.0418
	X17	Economic density	10^4 CNY·km^{-2}	0.0865
Resistance	X18	Construction capacity	-	0.0828
	X19	Road coverage ratio in built-up areas	%	0.0375
	X20	Density of drainage pipes in built-up areas	km/km^2	0.0404
	X21	Per capita park green space	$m^2/person^{-1}$	0.0232
	X22	Road density	km/km^2	0.0521
	X23	Length of road lighting	km/km^2	0.0455
	X24	Length of water supply pipes	km/km^2	0.0525
	X25	Gas penetration rate	%	0.0138
	X26	Communication skills		0.0487
	X27	Probability of geological hazards	-	0.0225
	X28	Density of geological hazards	-	0.0159

The classification of indicators into the three dimensions was based on their primary functions within the proposed resilience framework, although certain indicators may con-

tribute to more than one dimension. As the assessment relies on annual statistical data, the resulting indicators primarily represent potential adaptation, resistance, and recovery capacities rather than directly observed infrastructure performance, disaster losses, or post-disaster recovery processes.

3.2. Disaster Resilience Analysis

Table 3 presents the geological disaster resilience index calculated using the TOPSIS method. From 2018 to 2022, the overall level of geological disaster resilience in the study area exhibits a steadily increasing and stable upward trend. The regional average rises from 0.291 in 2018 to 0.372 in 2022, showing a notable cumulative increase and indicating continuous improvement in overall development. Meanwhile, the minimum value increases from 0.150 to 0.200, and the maximum value rises from 0.480 to 0.640, suggesting that both low- and high-level regions experience growth to varying degrees. These results indicate that geological disaster resilience in the study area does not exhibit overall deterioration, but rather shows a stable and positive evolutionary trend.

Table 3. Geological Disaster Resilience Index of Mountainous Cities in Western Sichuan Province.

Year	2018	2019	2020	2021	2022
BX	0.290	0.281	0.279	0.313	0.351
DB	0.164	0.199	0.187	0.208	0.243
DF	0.161	0.171	0.169	0.186	0.201
HY	0.484	0.539	0.567	0.590	0.639
JC	0.148	0.179	0.175	0.186	0.196
JL	0.177	0.198	0.181	0.196	0.224
KD	0.408	0.473	0.489	0.527	0.540
LX	0.261	0.247	0.269	0.308	0.315
LS	0.388	0.404	0.432	0.467	0.494
LH	0.170	0.175	0.174	0.181	0.205
LD	0.296	0.311	0.295	0.327	0.367
BK	0.259	0.291	0.305	0.332	0.337
MX	0.291	0.319	0.325	0.323	0.333
SM	0.445	0.454	0.499	0.534	0.538
TQ	0.398	0.411	0.434	0.492	0.516
WC	0.349	0.384	0.392	0.458	0.473
XJ	0.188	0.196	0.211	0.236	0.273
YG	0.437	0.474	0.493	0.522	0.556
YJ	0.207	0.245	0.274	0.259	0.268
Min	0.148	0.171	0.169	0.181	0.196
Max	0.484	0.539	0.567	0.590	0.639
Mean	0.291	0.313	0.324	0.350	0.372
Standard deviation	0.111	0.119	0.130	0.139	0.142
Skewness	0.274	0.423	0.410	0.323	0.383
Kurtosis	−1.335	−1.149	−1.159	−1.411	−1.229

From the perspective of dispersion and distribution characteristics, the standard deviation of the geological disaster resilience index increases from 0.111 in 2018 to 0.142 in 2022, showing a year-by-year expansion. This increase suggests significant differences in the extent of improvement among cities in terms of risk prevention capacity, infrastructure support, and comprehensive response capability. Some regions experience rapid improvement in resilience, while others progress more slowly, resulting in a widening gap in resilience levels across the study area. The skewness remains positive in all years, ranging from 0.274 to 0.423, indicating a right-skewed distribution of the resilience index. This implies that most cities are concentrated at low to medium levels, while high-value cities are relatively

few but exert a strong upward influence on the overall level. At the same time, kurtosis values are consistently negative, ranging from −1.15 to −1.41, suggesting a relatively flat distribution. This indicates that inter-city differences are not concentrated in a few extreme cases but are instead more evenly dispersed across the study area.

3.3. Temporal Trend Analysis

Based on the geological disaster resilience index calculated in Table 3, the temporal variation trends of resilience from 2018 to 2022 in the study area, along with the corresponding kernel density estimation (KDE) curves, were analyzed and visualized. The KDE calculation and visualization were implemented using MATLAB R2024b.

As shown in Figure 3, the average level of geological-hazard resilience exhibited an overall steady upward trend from 2018 to 2022. Although the resilience trajectories were broadly similar across the study period, the annual growth rate showed noticeable stage-specific fluctuations. Specifically, the growth rate decreased by 4.05 percentage points in 2020 and by 1.73 percentage points in 2022.

Figure 4 shows that, from 2018 to 2022, the kernel density distribution of geological-hazard resilience gradually shifted from lower-value ranges toward medium- and higher-value ranges. The overall kernel density surface progressively moved toward higher resilience levels, while probability density increasingly accumulated within the medium-value range. This pattern indicates that the improvement in geological-hazard resilience was not driven by only a small number of areas, but instead reflected a relatively broad-based improvement across the study area.

Further insights from the two-dimensional KDE profiles and three-dimensional surface plots reveal significant changes in both the peak height and position of the distribution across years. In 2018 and 2019, the KDE curves are relatively flat with no pronounced peaks, indicating a more dispersed distribution of resilience levels. From 2020 onward, the distribution gradually exhibits a clearer unimodal pattern, with increasing peak height, suggesting a growing concentration of regions at moderate resilience levels and a tendency toward structural convergence. However, in 2020, the increase in probability density within the high-value range is relatively constrained, and the tail extension weakens, indicating that resilience improvement during this period is limited by external shocks.

Moreover, throughout the study period, the resilience distribution does not exhibit a significant bimodal or multimodal structure, suggesting that a clear polarization pattern has not yet emerged across regions. Nevertheless, in 2021 and 2022, the probability density in the high-value range continues to increase, while that in the low-value range further contracts. This reflects an evolutionary pattern characterized by "low-end convergence and high-end expansion," with a gradual reduction in the number of low-resilience regions.

To further reveal the underlying causes of the significant disparities in geological disaster resilience, a systematic comparative analysis is conducted on the capacity characteristics of the three stages—adaptation, resistance, and recovery—over the period 2018–2022.

As shown in Figure 5, adaptive capacity exhibits an overall upward trend; however, there are significant inter-city differences in its evolution. Cities such as HY, KD, BK, LS, SM, TQ, and YG demonstrate relatively rapid improvements and maintain strong stability. In contrast, BX, DB, DF, JC, JL, LX, LH, and MX show slower growth, accompanied by more pronounced interannual fluctuations. HY and KD consistently rank among the top in adaptive capacity, exhibiting steady and sustained growth, which can be largely attributed to their higher levels of urbanization and more developed medical infrastructure. By comparison, LX shows the most significant decline in adaptive capacity during the study period. This decline is partly constrained by relatively limited medical resources and a high proportion of rural population, leading to insufficient public service provision and

restricted social support capacity, thereby weakening the city's ability to adapt to geological disasters and external uncertainties.

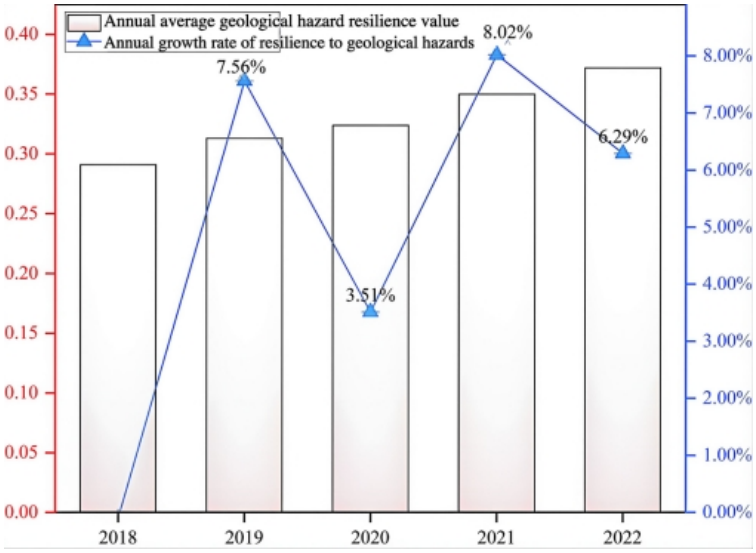

Figure 3. Temporal Evolution of Geological Disaster Resilience (2018–2022).

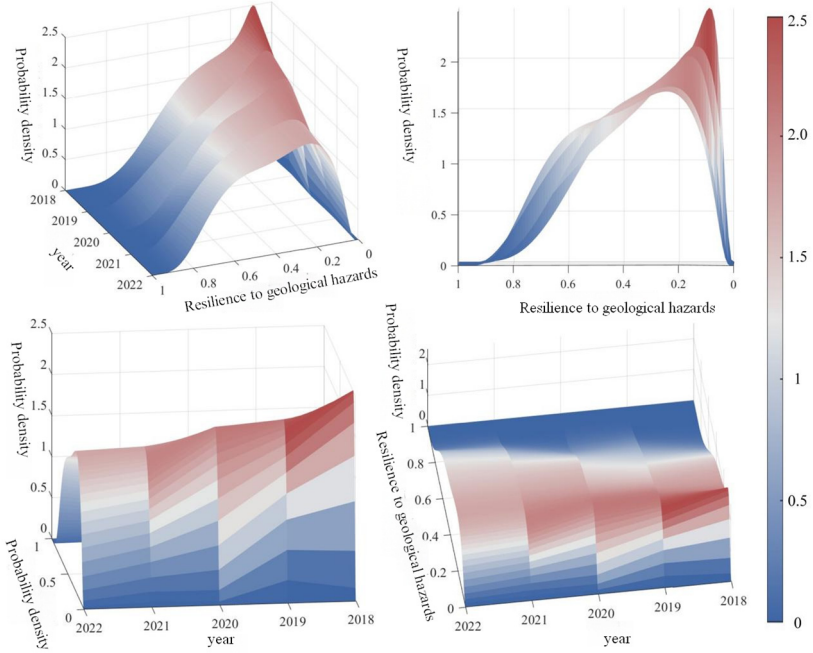

Figure 4. Kernel Density Estimation Curves of Geological Hazard Resilience (2018–2022).

According to Figure 6, although the overall level of resistance capacity in the study area is lower than that of adaptive and recovery capacities, the inter-city differences are relatively small. From a temporal perspective, the development of resistance capacity in most cities is not stable, exhibiting notable interannual fluctuations. This is closely related to the complex and unique geographical conditions of the study area. Specifically, the region is characterized by complex geological structures, large terrain variations, steep mountains, deep valleys, and dense gullies, all of which increase both the frequency and uncertainty of geological disasters. These conditions also significantly raise the difficulty of infrastructure construction and disaster prevention engineering. Rugged terrain not only prolongs construction cycles for infrastructure such as transportation but also constrains the

continuity and systematic implementation of engineering protection measures. As a result, it is difficult for some cities to achieve stable and sustained improvements in resistance capacity in the short term. Under such conditions, resistance capacity is more susceptible to disturbances from extreme climate events, sudden geological hazards, and interruptions in engineering projects, leading to pronounced stage-wise fluctuations. Nevertheless, with the continued advancement of China's Western Development Strategy, the resilience of key transportation node cities such as TQ, KD, WC, and XJ has improved rapidly, laying a foundation for subsequent coordinated regional development.

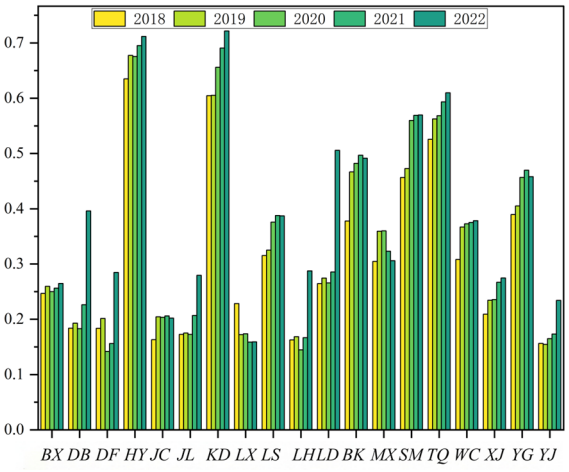

Figure 5. Changes in Adaptive Capacity of Mountainous Cities in Western Sichuan Province.

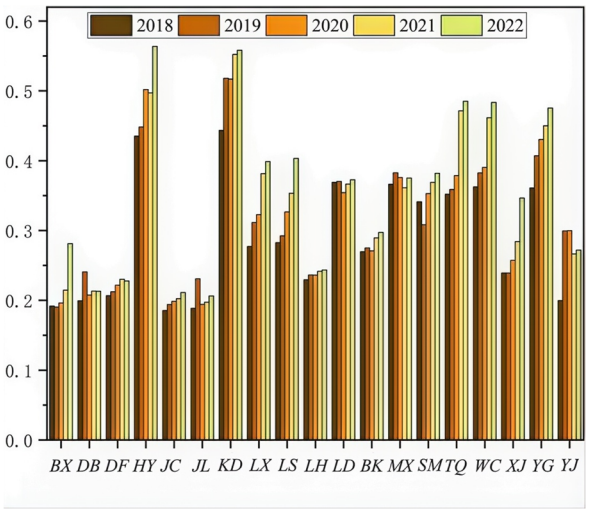

Figure 6. Changes in Resistance Capacity of Mountainous Cities in Western Sichuan Province.

As illustrated in Figure 7, recovery capacity exhibits the most pronounced inter-city disparities; however, its growth is more stable compared to adaptive and resistance capacities, with only a few cities showing significant fluctuations. Cities such as HY, LS, SM, and YG demonstrate the strongest recovery capacity. This is largely due to their transition from traditional resource-dependent economies toward more sustainable development models integrating "eco-industries," "specialized agriculture," and "all-for-one tourism," reflecting a dual characteristic of "resource-driven" and "ecology-oriented" development. In contrast, cities such as DB, DF, JC, LH, and XJ exhibit relatively weaker recovery capacity. Although these regions possess rich cultural and tourism resources and their industrial scales continue to expand, they generally face challenges such as reliance on a single dominant industry and the need for further optimization of industrial structure. The stability of economic

growth and risk resistance capacity in these areas still requires enhancement through the development of diversified industrial systems. Additionally, following the 2008 Wenchuan earthquake, WC initially relied on systematic post-disaster reconstruction and infrastructure development, and subsequently developed a dual-core economic system centered on specialized agriculture and cultural tourism. This transition has gradually reduced its dependence on reconstruction investment and further strengthened its economic resilience.

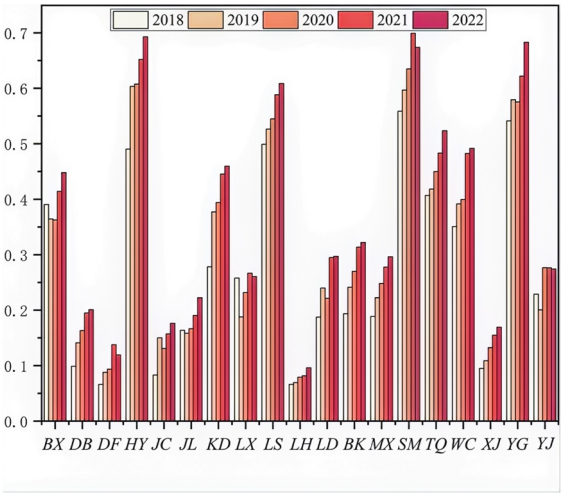

Figure 7. Changes in recovery capacity of mountainous cities in Western Sichuan Province.

3.4. Spatial Pattern Evolution

To examine interannual transitions in county-level geological disaster resilience states, this study employed the Jenks Natural Breaks classification method to classify 95 comprehensive resilience indices from 19 counties (county-level cities) over the period 2018–2022 using a unified classification scheme. This method identifies natural breakpoints in the data distribution by minimizing within-class variance, thereby classifying geological disaster resilience into three levels: low resilience (GRI $\leq$ 0.279), medium resilience (0.279 $<$ GRI $\leq$ 0.527), and high resilience (GRI $>$ 0.527). To ensure the comparability of resilience states across different years, consistent classification thresholds were applied throughout the entire study period to determine the resilience level of each county in each year.

By using Python 3.14.0 to process the geological disaster resilience classification data from 2018 to 2022, both the traditional Markov chain and the spatial Markov chain are calculated. According to the transition matrix of the traditional Markov chain shown in Figure 8, it can be observed that transitions between resilience levels in the study area occur relatively slowly, and downward transitions to lower levels may occur under certain conditions. Specifically, the probability of cities in low-resilience categories transitioning to medium-resilience levels is only 0.09. For cities in the medium-resilience category, the probability of downward transition to low resilience is 0.03, while the probability of upward transition to high resilience is 0.10. Cities in the high-resilience category tend to maintain their existing resilience level.

However, these findings are derived from the traditional Markov chain, which does not account for spatial dependence and thus cannot capture variations under different neighborhood resilience conditions. In other words, the results fail to reflect the potential spillover or radiation effects of high-resilience cities on neighboring medium- or low-resilience cities. Considering that Yu [52] finds that high-resilience cities exert a significant positive spillover effect on surrounding lower-resilience cities, this study further employs the spatial Markov chain to provide a more in-depth explanation of the observed transition dynamics.

By introducing spatial lag states into the Markov chain—i.e., constructing a spatial Markov chain—transition probability matrices under low-, medium-, and high-resilience neighborhood conditions are calculated and presented in Figure 9.

Under low-neighborhood conditions, geological disaster resilience exhibits a strong path dependence. Regions in a low-resilience state are primarily characterized by self-maintenance, with only a 0.06 probability of transitioning to a medium-resilience level, and virtually no possibility of directly upgrading to a high-resilience state. This indicates that, within low-resilience spatial environments, regional resilience is easily "locked in" by unfavorable surrounding conditions, making improvement particularly difficult.

At the same time, the medium-resilience state demonstrates a certain degree of stability, with zero probability of transitioning to other states. This suggests that under the constraints of low-resilience neighborhoods, medium-level resilience is neither prone to deterioration nor capable of further improvement due to insufficient driving forces. In addition, the high-resilience state is essentially absent under this neighborhood condition.

Under medium-neighborhood conditions, the evolutionary characteristics of geological disaster resilience show noticeable improvement compared to low-neighborhood contexts. Although low-resilience regions are still primarily characterized by state persistence, the probability of transitioning to medium resilience increases to 0.14, indicating that improvements in the surrounding environment can partially weaken the "lock-in effect" of low-resilience states. Meanwhile, the medium-resilience state remains highly stable, with a self-retention probability of 1. This suggests that medium resilience represents a stage of relative equilibrium rather than rapid transition. At the same time, the formation of high-resilience states remains limited, and high-resilience regions are essentially absent under this neighborhood condition.

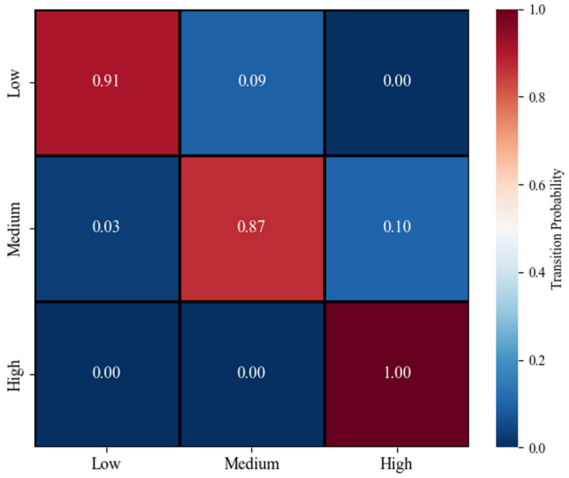

Figure 8. Traditional Markov transition probability matrix of geological-disaster resilience states from 2018 to 2022.

Under high-neighborhood conditions, the positive effect of spatial spillovers on geological disaster resilience becomes most evident. The probability of low-resilience regions transitioning to medium resilience further increases to 0.22, while the probability of remaining in the low-resilience state decreases to 0.78, demonstrating the significant promoting effect of favorable neighborhood environments on resilience improvement. Medium-resilience regions still tend to maintain their current state, but exhibit a 0.14 probability of transitioning to high resilience, indicating that under the influence of high-resilience neighborhoods, there exists a realistic possibility of upgrading from medium to high resilience. However, there is also a very small probability of downward transition from medium to low resilience, which may be attributed to the "siphoning effect" of high-resilience cities. Meanwhile,

high-resilience states exhibit strong stability, suggesting that once formed, high-resilience regions tend to be continuously reinforced through spatial agglomeration effects.

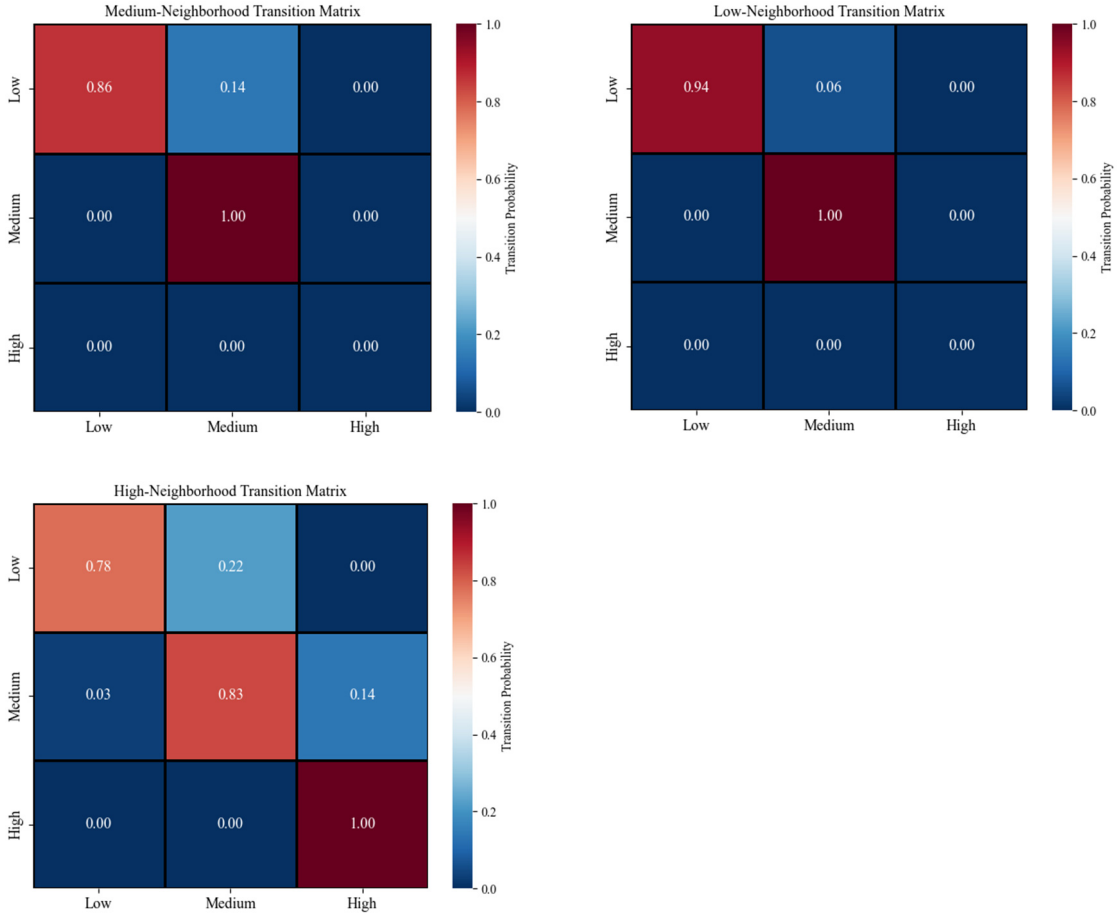

Figure 9. Spatial Markov transition probability matrices of geological-disaster resilience under different neighborhood resilience levels.

3.5. Spatial Network Analysis

3.5.1. Gravity-Based Connectivity Analysis

Using the calculated geological disaster resilience index and inter-city distances derived from ArcGIS 10.8, an improved gravity model is applied to compute the resilience-based gravitational values between cities, thereby providing a foundation for subsequent social network analysis. The urban gravity-based connectivity networks for 2018, 2020, and 2022 are illustrated accordingly.

Figure 10 shows that in 2018, a relatively strong resilience gravity network had already formed among SM, YG, TQ, BX, and LS. KD also exhibits medium to medium–high connectivity with these regions. LX, WC, and MX form a triangular structure, in which the connection between LX and WC is medium–high, while the connections between LX and MX, as well as between MX and WC, are at a medium level. Other regions are mainly characterized by low or medium–low resilience connections.

Figure 11 indicates that in 2020, the resilience gravity network was strengthened overall, and some low-level connections gradually evolved into medium–low connections. The resilience connection between XJ and KD as well as BK shifted from low to medium–low. Similarly, the connections between YJ and LD, YG, and HY also changed from low to medium–low. The connection between BK and JC improved from medium–low to medium. Due to its relatively remote geographical location, LH remains predominantly characterized

by low-level connections with other cities. In addition, the connectivity structure among cities in the southeastern part of the study area remains relatively stable, with no significant changes observed.

Figure 12 shows that by 2022, the resilience gravity network within the study area has improved significantly. Most inter-city connections have shifted from low to predominantly medium–low levels. The connection between XJ and BX improved from medium–low to medium, while the connection between YG and Lushan County increased from medium to medium–high. The connections between LH and both DF and BK also improved from low to medium–low. This spatial pattern further indicates that the evolution of the geological disaster resilience network in mountainous western Sichuan exhibits a clear stage-dependent characteristic. In 2018, resilience linkages were primarily constrained by geographic proximity and transportation accessibility, forming a "locally clustered but globally dispersed" network structure. Over time, inter-city resilience linkages gradually strengthened, with some low-level connections transitioning to medium–low levels, indicating a diffusion effect and a shift toward a more interconnected structure. By 2022, overall network connectivity had significantly improved, with a marked increase in medium–low and above connections, and several nodes forming relatively stable medium–high intensity linkages.

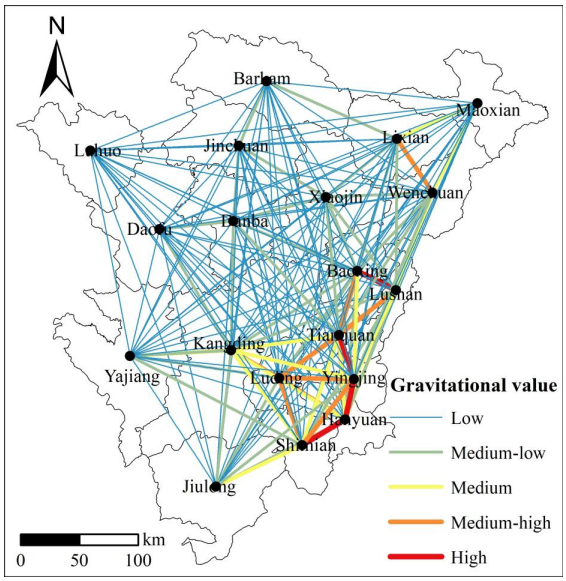

Figure 10. Geological Disaster Resilience Gravity Network of Mountainous Cities in Western Sichuan, 2018.

3.5.2. Network Structure Analysis

According to the binarization rule defined in Section 2.2.4, the continuous gravity values $F_{ij,t}$ were converted into a directed adjacency matrix A_t. Using the same threshold criterion, potential resilience association networks were constructed for 2018, 2020, and 2022, respectively, and the network density, number of links, out-degree centrality, and in-degree centrality were subsequently calculated.

The gravity values calculated using the improved gravity model are converted into a binary gravity matrix, which is then used as the foundational dataset for social network analysis. The binary matrix is imported into UCINET 6 software to compute and visualize the network characteristics of inter-city geological disaster resilience within the study area.

As shown in Table 4, the network density of the geological disaster resilience network increases steadily over time, with a total growth rate of 48.88% and an absolute increase of 0.197. Specifically, from 2018 to 2020, network density rises from 0.403 to 0.480, an increase of 0.077, corresponding to a growth rate of 19.11%. From 2020 to 2022, it further increases

from 0.480 to 0.600, with an increment of 0.120 and a growth rate of 25.00%. In parallel, the total number of network connections increases by 68, representing a growth rate of 49.28%. From 2018 to 2020, the number of connections grows from 138 to 164, an increase of 26 (18.84%). From 2020 to 2022, it further increases from 164 to 206, an increment of 42 (25.61%).

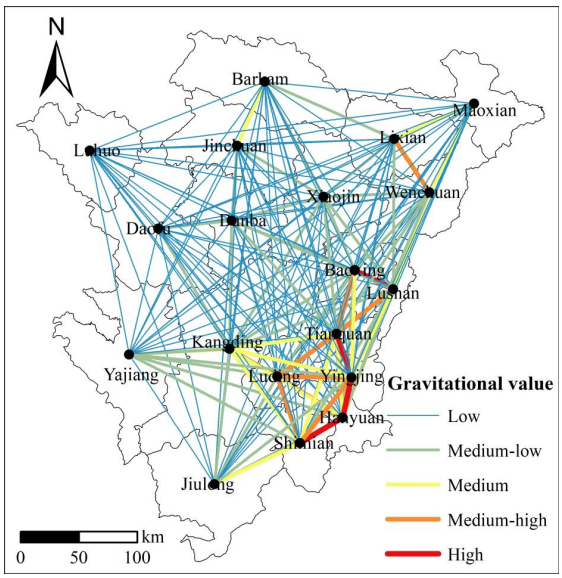

Figure 11. Geological Disaster Resilience Gravity Network of Mountainous Cities in Western Sichuan, 2020.

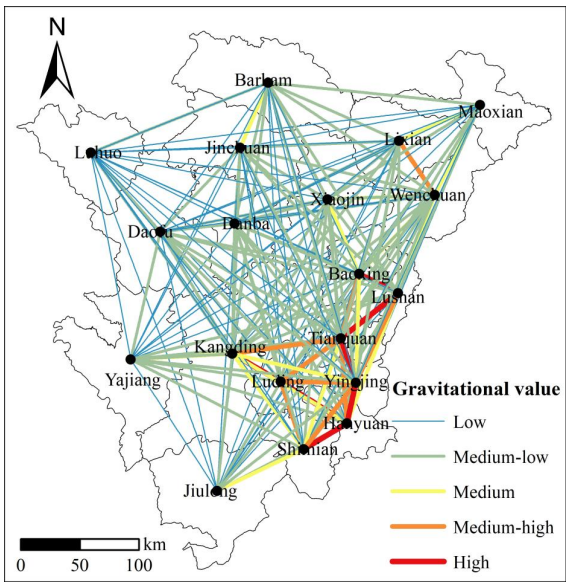

Figure 12. Geological Disaster Resilience Gravity Network of Mountainous Cities in Western Sichuan, 2022.

Table 5 shows that both out-degree centrality and in-degree centrality of cities within the resilience network exhibit a continuous upward trend, indicating increasingly dense inter-city resilience linkages and significantly enhanced regional coordination. In 2018, most cities still display relatively low to medium levels of centrality, and the overall network structure remains sparse. By 2020, driven by increasing regional demand for coordinated disaster prevention, the in-degree centrality of most cities increases markedly, and network connectivity begins to strengthen. By 2022, both out-degree and in-degree centralities

rise simultaneously, indicating a transition from unilateral dependence to bidirectional interaction. Overall, the network evolves from a dispersed and weakly connected structure toward a more clustered and strongly connected configuration.

Table 4. Linkage strength of the geological disaster resilience network.

Year	Network Density	Number of Connections
2018	0.403	138
2020	0.480	164
2022	0.600	206

Table 5. Centrality of the geological disaster resilience network.

Study Area	2018		2020		2022	
	Out-Degree Centrality	In-Degree Centrality	Out-Degree Centrality	In-Degree Centrality	Out-Degree Centrality	In-Degree Centrality
BX	11	11	11	12	15	13
DB	3	10	5	13	11	15
DF	2	4	2	6	5	14
HY	11	8	13	10	14	10
JC	3	4	4	7	5	11
JL	3	6	4	7	5	7
KD	13	8	15	11	17	13
LX	7	7	7	10	9	11
LS	12	11	14	11	16	12
LH	1	1	1	1	2	4
LD	9	9	10	10	13	11
BK	4	5	6	6	9	10
MX	6	3	6	4	6	8
SM	9	8	11	9	13	10
TQ	14	8	14	10	17	12
WC	9	9	13	11	14	13
XJ	7	12	8	12	12	14
YG	12	8	13	8	15	10
YJ	2	6	7	6	8	8

In Figure 13, from the perspective of nodal structural evolution, the study area gradually forms a hierarchical network characterized by a core–diffusion–growth–periphery structure. KD, TQ, Lushan County, BX, and WC exhibit consistently high and significantly increasing in-degree and out-degree centralities, establishing themselves as core hubs with both resource export and factor aggregation functions. These nodes constitute the key foundation for network stability (e.g., KD out-degree increases from 13 to 17, and its in-degree rises from 8 to 13).

HY, YG, and SM are characterized by relatively higher out-degree centrality, indicating their dominant diffusion function and their role as important channels for network circulation. DB, DF, XJ, JC, and BK show faster growth in in-degree than out-degree, forming typical "absorption-oriented" nodes (e.g., DF in-degree increases from 4 to 14, while its out-degree rises only from 2 to 5). This pattern suggests that improvements in their resilience rely more heavily on external resource inflows, while their outward diffusion capacity remains limited. Among them, DB and XJ, although already deeply embedded in the network, have not yet developed stable outward-acting capabilities.

Overall, this differentiation reflects a certain degree of path dependence on external support in regions with high disaster exposure or relatively weak foundational conditions.

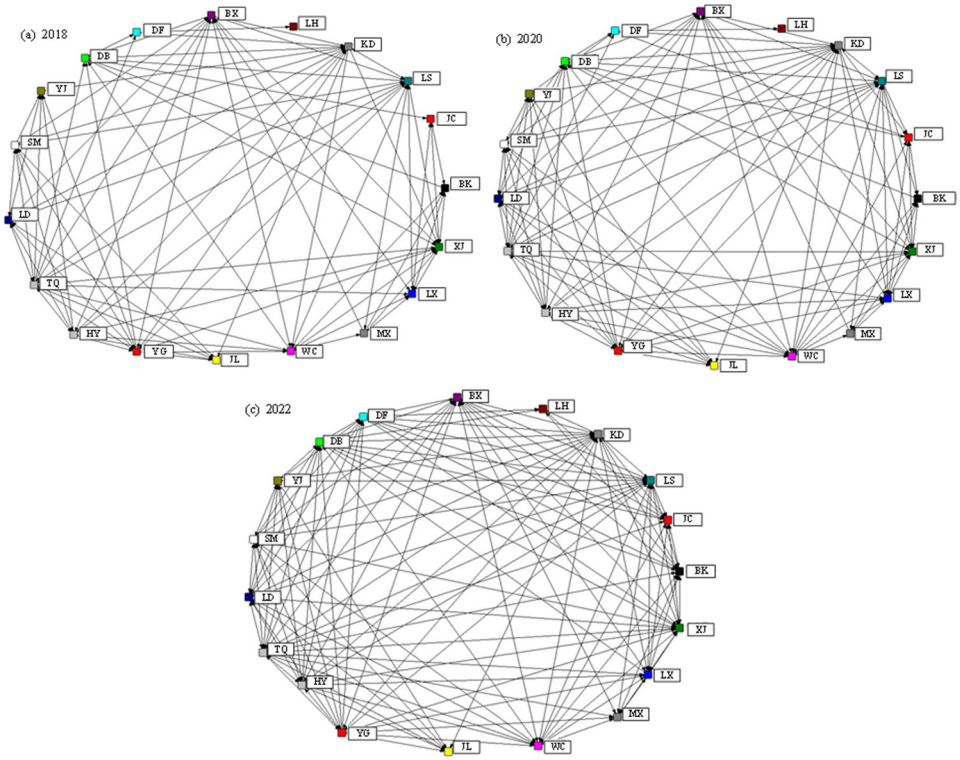

Figure 13. (**a**) 2018, (**b**) 2020, and (**c**) 2022 partial association networks of geological disaster resilience.

LH, JL, YJ, and MX remain persistently characterized by low out-degree and low in-degree centrality, exhibiting a pronounced marginalization within the network structure. Taking LH as an example, its centrality remains at the lowest level in both 2018 and 2020, and although it shows some improvement by 2022, it is still significantly below the regional average. This indicates a relatively low level of participation in the regional resilience coordination network. Such cities are often constrained by remote geographic location, limited transportation accessibility, and insufficient public service provision, which hinders their effective integration into regional coordination systems and results in structural constraints on resilience enhancement.

In Table 6 and Figure 14, from a temporal evolution perspective, the regional resilience network shifts from an early-stage concentrated structure dominated by a few nodes toward a more networked structure characterized by multi-node collaboration. In 2018, network linkages are highly concentrated in a small number of core cities. By 2020, driven by external shocks and increasing coordination demand, the in-degree of medium- and low-centrality nodes increases, and the network begins to densify. By 2022, multiple nodes with both high out-degree and high in-degree emerge, forming a multi-centric network structure centered on KD, TQ, LS, BX, and WC, indicating that regional resilience improvement increasingly depends on cross-regional coordination effects.

Based on nodal in-degree and out-degree characteristics, cities can be classified into four categories: core nodes (strong bidirectional hubs), diffusion-oriented nodes (outward-dominant), growth-oriented nodes (inward-dependent), and peripheral nodes (low participation). Overall, the geological disaster resilience network in the study area is evolving from localized agglomeration toward a multi-node, hierarchically structured network. However, due to terrain complexity and spatial distance constraints, high-intensity cross-regional coordination remains insufficient, and the network structure still has room for optimization. This evolutionary process also confirms the effectiveness of social network analysis in characterizing regional resilience structures.

Table 6. Node classification of geological disaster resilience networks.

Node Types	Study Area	Classification Criteria
Core node	KD TQ LS	Both out-degree and in-degree are higher than the mean value.
Diffusion node	BX WC HY YG SM	Out-degree is above the mean value, while in-degree is below the mean value.
Growth node	DB DF XJ BK	In-degree grows faster than out-degree, indicating a significant improvement in absorptive capacity.
Periphery node	JC LX LD LH JL YJ MX	Both out-degree and in-degree are below the mean.

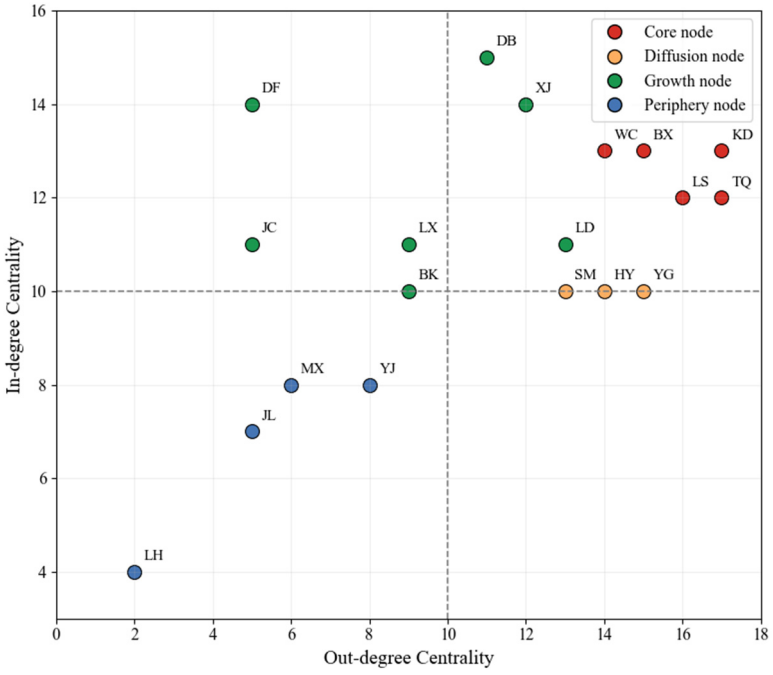

Figure 14. Two-Dimensional Quadrant Plot of Network Node Distribution.

4. Discussion

4.1. Main Findings and Practical Implications

This study systematically examined the evolution of geological disaster resilience across 19 mountainous counties in western Sichuan Province from 2018 to 2022, based on a three-dimensional assessment framework comprising adaptation, resistance, and recovery capacities, combined with spatiotemporal evolution analysis, Markov chain analysis, and social network analysis. The results indicate that the overall level of geological disaster resilience in the study area exhibited an upward trend, while disparities among counties

continued to widen to some extent, reflecting the coexistence of overall improvement and regional differentiation.

Regarding spatial disparities, the resilience differentiation observed among mountainous counties in this study is broadly consistent with findings from previous research on disaster resilience in mountainous regions. For example, a study of landslide resilience in mountainous areas of Chongqing identified pronounced center–periphery disparities in social resilience, with areas characterized by relatively concentrated economic resources and public services generally exhibiting higher resilience levels, while peripheral areas demonstrated comparatively weaker resilience conditions [53]. Another study examining the spatiotemporal evolution of landslide resilience in Chongqing from 2010 to 2020 similarly highlighted the coexistence of resilience improvement and regional disparities in mountainous cities, emphasizing the need to coordinate economic development with disaster response capacity [30]. In the present study, eastern counties and some counties with relatively favorable infrastructure conditions exhibited higher levels of comprehensive resilience, whereas certain western counties showed relatively lower resilience levels and more limited improvements. These findings are generally consistent with the spatial heterogeneity of mountainous-region resilience reported in previous studies. Considering the geological background of the study area, the mountainous region of western Sichuan is located along the eastern margin of the Tibetan Plateau and encompasses different tectonic units, including the Longmenshan Fault Zone, the Xianshuihe Fault Zone, and the Songpan–Ganzi Orogenic Belt. These areas exhibit pronounced differences in topographic relief, valley incision, and engineering construction conditions. Complex terrain and geological structures are not only associated with the spatial distribution of geological hazards but may also be related to differences in county-level resilience conditions by constraining land availability for development, affecting transportation accessibility, and increasing the difficulty of infrastructure construction. Nevertheless, geological structures and topographic conditions are not the sole determinants of comprehensive resilience, as counties in the study area also differ in their socioeconomic foundations, public service resources, and infrastructure support conditions.

Regarding the internal structure of resilience, adaptation, resistance, and recovery capacities exhibited distinct evolutionary characteristics. Adaptation and recovery capacities generally improved, whereas resistance capacity remained relatively weak, with noticeable interannual fluctuations in some counties. These findings indicate that improvements across the three resilience dimensions were uneven and that internal disparities among capacities persisted despite the overall increase in comprehensive resilience. In terms of indicator composition, adaptation capacity primarily encompasses demographic structure, social security, and healthcare services; recovery capacity mainly reflects regional economic foundations, fiscal resources, and industrial development conditions; and resistance capacity is closely associated with infrastructure support and geological hazard levels. In the mountainous region of western Sichuan, complex terrain and geological conditions may increase the difficulty of constructing transportation infrastructure, municipal facilities, and geological disaster mitigation projects, thereby constituting important practical constraints on improvements in resistance capacity. These findings suggest that enhancing resilience in mountainous counties requires attention not only to socioeconomic development and improvements in public services but also to the relationship between infrastructure support capacity and geological hazard levels.

Regarding temporal evolution, the traditional Markov chain results indicate that different resilience levels in the study area exhibited relatively high state persistence, while the probability of low-resilience counties transitioning to higher resilience levels remained relatively limited. The spatial Markov chain analysis further revealed differences in tran-

sition probabilities under different neighborhood resilience conditions. In low-resilience neighborhoods, low-resilience states exhibited relatively high self-transition probabilities. In contrast, under high-resilience neighborhood conditions, counties with low and medium resilience levels showed relatively higher probabilities of upward transitions. These results indicate a certain statistical association between changes in county-level resilience states and neighborhood resilience conditions, suggesting that the evolution of regional resilience exhibits spatial association characteristics.

Regarding spatial network characteristics, the potential resilience association network constructed using the modified gravity model exhibited a gradual increase in connectivity, accompanied by increases in the number of network connections and overall network density. Some counties also gradually developed relatively prominent positions in terms of network centrality. These findings indicate that, under the specified gravity model and network construction rules, potential resilience associations among counties in the study area became stronger, although pronounced spatial disparities remained within the network structure. Specifically, some counties with relatively high comprehensive resilience and favorable geographical conditions exhibited higher network centrality, whereas certain western counties continued to show relatively low levels of network embeddedness. Considering the geographical characteristics of the study area, mountainous terrain and spatial distance may impose constraints on potential intercounty connections, resulting in a network structure characterized by the coexistence of increasing overall connectivity, localized clustering, and peripheral differentiation.

These findings provide implications for geological disaster risk governance and territorial spatial planning in the mountainous region of western Sichuan. First, given the overall improvement in comprehensive resilience alongside widening regional disparities, greater attention should be paid to strengthening infrastructure support and public service capacities in low-resilience counties to prevent differences in regional development conditions from further translating into disparities in disaster response capacity. Second, considering the relatively weak resistance capacity, geological hazard assessment should be more closely integrated with transportation, municipal infrastructure, and emergency facility planning. Infrastructure site selection should comprehensively consider geological safety, transportation accessibility, and network redundancy to reduce the dependence of critical infrastructure on high-hazard areas and single transportation corridors. Finally, considering the spatial differentiation of the potential resilience association network, counties with relatively high network centrality could be prioritized as coordination nodes for interregional disaster prevention and mitigation cooperation. Meanwhile, greater emphasis should be placed on improving transportation connections, emergency support, and resource accessibility in peripheral counties to promote the coordinated enhancement of disaster response capacities across mountainous counties.

4.2. Limitations and Future Research

Although this study investigates the dynamic evolution of geological-hazard resilience in mountainous counties of western Sichuan from three perspectives—resilience level, state transition, and spatial association networks—several limitations should be acknowledged.

First, the resilience assessment is primarily based on annual statistical data from 2018 to 2022, with county-level composite resilience indices constructed using social, economic, infrastructural, and hazard-related indicators. Although this approach can characterize the overall resilience capacity of different counties in a given year, annual indicators are unable to capture high-frequency dynamic changes in system functionality, emergency response, and recovery following individual geological-hazard events.

Second, the study period and the number of state-transition observations are relatively limited. The analysis covers only 2018–2022, during which the 19 study units generate 76 potential state-transition observations across four consecutive annual intervals. After further conditioning the spatial Markov analysis on neighborhood resilience states, the number of observations available for some transition types becomes even smaller.

Third, the composite assessment results remain dependent on indicator selection, weighting, and aggregation methods. The entropy weight method determines indicator weights based on their dispersion within the study sample, thereby reducing direct subjective intervention; however, the resulting weights remain sensitive to sample distributions and indicator variability. TOPSIS further aggregates multidimensional information into a composite index, which may obscure non-compensatory differences among different resilience dimensions.

Future research could further employ spatial panel models, quasi-experimental designs, or other appropriate mechanism-identification approaches to independently examine the direction, magnitude, and spatial heterogeneity of the effects of different factors on changes in resilience.

5. Conclusions

This study assessed geological-hazard resilience across 19 mountainous counties in western Sichuan Province using an adaptation–resistance–recovery framework. The main conclusions are as follows:

(1) Overall geological-hazard resilience increased from 2018 to 2022, with the mean resilience index rising from 0.291 to 0.372. However, the increasing standard deviation indicates that regional disparities widened during the study period.
(2) Adaptation and recovery capacities generally improved, whereas resistance capacity remained comparatively weak and showed greater interannual fluctuations. The resilience distribution shifted toward higher values, but the simultaneous compression of the lower-value tail and expansion of the upper-value tail indicate asymmetric improvement rather than overall regional convergence.
(3) Markov analysis showed relatively high persistence among low-resilience areas, while upward transition probabilities varied across neighborhood conditions. Meanwhile, the potential resilience association network became increasingly connected, with higher network density and stronger inter-county linkages. KD, TX, LS, BX, and WC occupied relatively central network positions, whereas LH, JL, YJ, and MX remained peripheral.

This study provides a multi-level perspective linking resilience levels, state transitions, and spatial association structures, and offers evidence for differentiated disaster-risk reduction and regional resilience planning in mountainous areas.

Author Contributions: Conceptualization, H.Y.; Methodology, K.M. and Y.L.; Software, K.M. and Y.L.; Investigation, K.M.; Data curation, Y.L.; Writing—original draft, K.M. and Y.L.; Writing—review & editing, K.M. and Y.L.; Visualization, K.M.; Project administration, Y.L. All authors have read and agreed to the published version of the manuscript.

Funding: We gratefully acknowledge the financial support provided by the Talent Recruitment Program of Xihua University through the project "Research on Multifactor Coupled Risks and Resilience Enhancement Pathways for Megacity Infrastructure under Extreme Natural Disasters" (Grant No. Z242110), and by the Research Center for Social Development and Social Risk Control, a Key Research Base of Philosophy and Social Sciences in Sichuan Province, through the project "Multi-factor Coupling Risk and Resilience Improvement Paths of Urban-Rural Infrastructure Under Extreme Natural Disasters" (Grant No. SR24A11).

Institutional Review Board Statement: Not applicable.

Informed Consent Statement: Not applicable.

Data Availability Statement: The data presented in this study are available on request from the authors.

Conflicts of Interest: The authors declare no conflicts of interest.

References

1. Carlson, C.J.; Mitchell, D.; Gibb, R.; Stuart-Smith, R.F.; Carleton, T.; Lavelle, T.E.; Lippi, C.A.; Lukas-Sithole, M.; North, M.A.; Ryan, S.J.; et al. Health Losses Attributed to Anthropogenic Climate Change. *Nat. Clim. Change* **2025**, *15*, 1052–1055. [CrossRef] [PubMed]
2. Huang, L.; Wang, J.; Lu, Y.; Ye, Y.; Zhai, T. Measuring the Resilience of Mountain City Ecological Network: A Methodological Framework Integrating Real Disaster Shocks and Simulated Disturbance Scenarios. *J. Environ. Manag.* **2025**, *384*, 125573. [CrossRef] [PubMed]
3. Yin, H.; Xiang, Y.; Fan, Q.; Ao, Y.; Chen, D. Disaster Resilience Assessment and Key Drivers of Resilience Evolution in Mountainous Cities Facing Geo-Disasters: A Case Study of Disaster-Prone Counties in Western Sichuan. *Sustainability* **2025**, *17*, 3291. [CrossRef]
4. Fan, G.; Lin, Z.; Zhou, J. Failure Parameter Inversion of the Baige Landslides Based on Seismic Signal Analysis. *Environ. Earth Sci.* **2025**, *84*, 239–260. [CrossRef]
5. Daud, H.; Tanoli, J.I.; Asif, S.M.; Qasim, M.; Ali, M.; Khan, J.; Bhatti, Z.I.; Jadoon, I.A.K. Modelling of Debris-Flow Susceptibility and Propagation: A Case Study from Northwest Himalaya. *J. Mt. Sci.* **2024**, *21*, 201–217. [CrossRef]
6. Ewa, W.O.; Ugwu, O.O. Security Vulnerability Assessments for Sustainable Infrastructure: A Scientometric Review. *Environ. Dev. Sustain.* **2026**, *28*, 28031–28064. [CrossRef]
7. Leone, M.F.; Zuccaro, G.; De Gregorio, D.; Turchi, A.; Tedeschi, A.; Büegelmayer-Blaschek, M.; Sfetsos, A.; Zarikos, I.; Coronas, A.D.L.C.; Russo, B. A Holistic Asset-Level Modelling Framework for a Comprehensive Multi-Hazard Risk/Impact Assessment: Insights from the ICARIA Project. *Int. J. Disaster Risk Reduct.* **2025**, *119*, 105319. [CrossRef]
8. Martínez-Sepúlveda, M.; Martí, J.; López-Saavedra, M. VOLCANBOX: A Software Platform for Volcanic Hazard Assessment. *Int. J. Disaster Risk Reduct.* **2024**, *113*, 104817. [CrossRef]
9. Duo, E.; Fernández-Montblanc, T.; Armaroli, C. Semi-Probabilistic Coastal Flood Impact Analysis: From Deterministic Hazards to Multi-Damage Model Impacts. *Environ. Int.* **2020**, *143*, 105884. [CrossRef] [PubMed]
10. Zhang, H.; Meng, C.; Wang, Y.; Wang, Y.; Li, M. Comprehensive Evaluation of the Effects of Climate Change and Land Use and Land Cover Change Variables on Runoff and Sediment Discharge. *Sci. Total Environ.* **2020**, *702*, 134401. [CrossRef] [PubMed]
11. Lin, X.; Zhang, S.; Zhao, X.; Li, R.; Wang, S.; Yang, L.; Chen, X. Global Thresholds for the Climate-Driven Effects of Vegetation Restoration on Runoff and Soil Erosion. *J. Hydrol.* **2025**, *647*, 132374. [CrossRef]
12. Bunel, R.; Lecoq, N.; Copard, Y.; Massei, N. Effects of Climate Variability Changes on Runoff and Erosion in the Western European Loess Belt Region (NW, France). *Sci. Total Environ.* **2023**, *903*, 166536. [CrossRef] [PubMed]
13. Wu, C.-H.; Chen, S.-C. Determining Landslide Susceptibility in Central Taiwan from Rainfall and Six Site Factors Using the Analytical Hierarchy Process Method. *Geomorphology* **2009**, *112*, 191–204. [CrossRef]
14. Lee, S.; Jang, J.; Kim, Y.; Cho, N.; Lee, M.-J. Susceptibility Analysis of the Mt. Umyeon Landslide Area Using a Physical Slope Model and Probabilistic Method. *Remote Sens.* **2020**, *12*, 2663. [CrossRef]
15. Zou, Q.; Jiang, H.; Cui, P.; Zhou, B.; Jiang, Y.; Qin, M.; Liu, Y.; Li, C. A New Approach to Assess Landslide Susceptibility Based on Slope Failure Mechanisms. *CATENA* **2021**, *204*, 105388. [CrossRef]
16. Guo, Z.; Huang, Q.; Yu, D.; Liu, Y.; Xu, M.; Xie, Q. Hydrological and Failure Process of Loess-Bedrock Fill Slopes under Continuous Heavy Rainfall. *J. Rock Mech. Geotech. Eng.* **2025**, *17*, 7208–7220. [CrossRef]
17. Arabameri, A.; Saha, S.; Roy, J.; Tiefenbacher, J.P.; Cerda, A.; Biggs, T.; Pradhan, B.; Thi Ngo, P.T.; Collins, A.L. A Novel Ensemble Computational Intelligence Approach for the Spatial Prediction of Land Subsidence Susceptibility. *Sci. Total Environ.* **2020**, *726*, 138595. [CrossRef] [PubMed]
18. Gupta, V.; Choudhary, R.; Agarwal, A. Integrating Land Use and Traffic to Spatial Prediction of Particulate Matter. *Urban Clim.* **2024**, *54*, 101844. [CrossRef]
19. Karimzadeh, S.; Matsuoka, M.; Kuang, J.; Ge, L. Spatial Prediction of Aftershocks Triggered by a Major Earthquake: A Binary Machine Learning Perspective. *ISPRS Int. J. Geo-Inf.* **2019**, *8*, 462. [CrossRef]
20. Pandey, A.; Mondal, C.; Sastry, B.S. Multiple Logistic Regression Based Prediction of Heat Flow Direction in an Intake Incline of Shallow Depth by Integrating Thermal Flywheel Effect: A Case Study. *Appl. Therm. Eng.* **2022**, *213*, 118765. [CrossRef]
21. Kumar Bhagat, N.; Mishra, A.K.; Singh, R.K.; Sawmliana, C.; Singh, P.K. Application of Logistic Regression, CART and Random Forest Techniques in Prediction of Blast-Induced Slope Failure during Reconstruction of Railway Rock-Cut Slopes. *Eng. Fail. Anal.* **2022**, *137*, 106230. [CrossRef]

22. Jiang, X.; Wen, T.; Li, P.; Zhang, Z.; Wu, M.; Liu, X.; Chen, P. Prediction Model of Outburst Debris Flow Triggered by Landslide Dam Failure Considering the Erosion Process. *Comput. Geotech.* **2023**, *158*, 105326. [CrossRef]
23. Robles-Velasco, A.; Cortés, P.; Muñuzuri, J.; Onieva, L. Prediction of Pipe Failures in Water Supply Networks Using Logistic Regression and Support Vector Classification. *Reliab. Eng. Syst. Saf.* **2020**, *196*, 106754. [CrossRef]
24. Jin, T.; Hu, X.; Liu, B.; Xi, C.; He, K.; Cao, X.; Luo, G.; Han, M.; Ma, G.; Yang, Y.; et al. Susceptibility Prediction of Post-Fire Debris Flows in Xichang, China, Using a Logistic Regression Model from a Spatiotemporal Perspective. *Remote Sens.* **2022**, *14*, 1306. [CrossRef]
25. Zhan, J.; Yao, Z.; Shen, Y.; Huang, D.; Yu, Z.; Peng, J. Sediment Transport Evolution and Impact on Vegetation Recovery in the Hanping Village Landslide–Debris Flow Disaster Chain in Shaanxi, China. *Ecol. Eng.* **2025**, *219*, 107718. [CrossRef]
26. Tonetto, J.L.; Pique, J.M.; Rapetti, C. Multiple Hazards and Economic Resilience: Sectoral Impacts and Post-Disaster Recovery in a High-Risk Brazilian State. *Sustainability* **2025**, *17*, 7711. [CrossRef]
27. Luo, Z.; Yang, J.; Huang, B.; Chen, W.; Gao, Y.; Meng, Q. Reconstruction and Visualization of Landslide Events Based on Pre- and Post-Disaster Remote Sensing Data. *Water* **2023**, *15*, 2023. [CrossRef]
28. Marchetti, N.; Newnham, E.; Robinson, D.E. The Resilience Paradox: Rural Self-Reliance and the Limits of Disaster Recovery. *Int. J. Disaster Risk Reduct.* **2025**, *127*, 105660. [CrossRef]
29. Lin, Y.; Xiang, Y.; Yin, H.; Chen, Z. Selection of Emergency Logistics Facility Locations Considering Major Natural Disasters in Mountainous Cities Based on GIS-MCDM. *Sci. Rep.* **2026**, *16*, 11634. [CrossRef] [PubMed]
30. Wen, H.; Huang, J.; Qian, L.; Li, Z.; Zhang, Y.; Zhang, J. The Spatial-Temporal Evolution Patterns of Landslide-Oriented Resilience in Mountainous City: A Case Study of Chongqing, China. *J. Environ. Manag.* **2024**, *370*, 122963. [CrossRef] [PubMed]
31. Wang, J.; Kang, Y.; Feng, B. Disaster Resilience in the Geohazard-Prone Mountainous Areas: Evidence from the Hengduan Mountain, Southwest China. *Int. J. Disaster Risk Reduct.* **2025**, *119*, 105331. [CrossRef]
32. Zhu, H.; Zhu, X.; Li, Y.; Ao, Y.; Jia, X.; Peng, P.; Li, M.; Li, J. The Spatiotemporal Evolution of Geo-Disaster Resilience in China and the Impact Mechanism of Environmental Governance. *Atmosphere* **2025**, *16*, 247. [CrossRef]
33. Hosseini, S.; Barker, K.; Ramirez-Marquez, J.E. A Review of Definitions and Measures of System Resilience. *Reliab. Eng. Syst. Saf.* **2016**, *145*, 47–61. [CrossRef]
34. Wei, Y.; Cheng, Y.; Liao, H. Optimal Resilience-Based Restoration of a System Subject to Recurrent Dependent Hazards. *Reliab. Eng. Syst. Saf.* **2024**, *247*, 110137. [CrossRef]
35. Wei, Y.; Cheng, Y.; Liao, H.; Elsayed, E.A. Resilience Modeling for an Engineered Network with Multimodal Performance under Multiple Recurrent Hazards. *Reliab. Eng. Syst. Saf.* **2026**, *266*, 111640. [CrossRef]
36. Choo, M.; Yoon, D.K. A Meta-Analysis of the Relationship between Disaster Vulnerability and Disaster Damage. *Int. J. Disaster Risk Reduct.* **2024**, *102*, 104302. [CrossRef]
37. Li, T.; Song, F.; De Cock, A.; De Maeyer, P.; Bao, J.; Yuan, Y.; Naibi, S.; Bao, A.; Ho, L.T.; Goethals, P. Global Disparities in Rural and Urban Population Exposure to Compound Drought and Heatwave Events. *npj Clim. Atmos. Sci.* **2025**, *8*, 207–217. [CrossRef]
38. Kadir, S.B. Viewing Disaster Resilience through Gender Sensitive Lens: A Composite Indicator Based Assessment. *Int. J. Disaster Risk Reduct.* **2021**, *62*, 102398. [CrossRef]
39. Fonseca, F.; Ribeiro, P.J.G. A Multidimensional Spatial Framework for Assessing Territorial Resilience across 86 Municipalities in Northern Portugal. *Land* **2026**, *15*, 1082. [CrossRef]
40. Pratiwi, I.D.; Chusnayah, F. The Intersection of Population Growth and Disaster Vulnerability in Cangkringan District. *IOP Conf. Ser. Earth Environ. Sci.* **2025**, *1462*, 12045. [CrossRef]
41. Levy, D.M.; Kottler, J.A.; Adams, J.W.; Crawford, J.R.; Levy, M.L. Using a Hybrid Approach to Increase the Impact of Medical Response to Natural Disasters. *Disaster Med. Public Health Prep.* **2023**, *17*, e303. [CrossRef] [PubMed]
42. Keim, M.E.; Smith, T.M.; Burkle, F.M. The Annual Global Incidence Rate of Extreme Weather Event Disasters Appears Positively Correlated with World GDP, 1961–2020. *Prehospital Disaster Med.* **2022**, *37*, 431–436. [CrossRef] [PubMed]
43. Kato, H.; Okubo, T. The Resilience of FDI to Natural Disasters through Industrial Linkages. *Environ. Resour. Econ.* **2022**, *82*, 177–225. [CrossRef]
44. Liu, A.; Li, Z.; Shang, W.-L.; Ochieng, W. Performance Evaluation Model of Transportation Infrastructure: Perspective of COVID-19. *Transp. Res. Part A Policy Pract.* **2023**, *170*, 103605. [CrossRef] [PubMed]
45. Boakye, J.; Guidotti, R.; Gardoni, P.; Murphy, C. The Role of Transportation Infrastructure on the Impact of Natural Hazards on Communities. *Reliab. Eng. Syst. Saf.* **2022**, *219*, 108184. [CrossRef]
46. Opabola, E.A.; Galasso, C. Informing Disaster-Risk Management Policies for Education Infrastructure Using Scenario-Based Recovery Analyses. *Nat. Commun.* **2024**, *15*, 325–337. [CrossRef] [PubMed]
47. Wu, B.; Wang, W.; Tan, Z.; Ding, D. Resilience Modeling for Discrete-Time Multi-State Systems Based on Aggregated Markov Chains. *Reliab. Eng. Syst. Saf.* **2025**, *264*, 111426. [CrossRef]

48. Hou, B.; Zhang, J.; Ma, T.; Miao, H.; Xu, C.; Du, X. Exploring Infrastructure Dependence on Community Environment under Natural Hazards: Quantifying the Impact of Building Destruction on Infrastructure Functionality. *Int. J. Disaster Risk Reduct.* **2026**, *133*, 105935. [CrossRef]
49. Hong, B.; Shao, B.; Wang, B.; Zhao, J.; Qian, J.; Guo, J.; Xu, Y.; Li, C.; Zhu, B. Using the Meteorological Early Warning Model to Improve the Prediction Accuracy of Water Damage Geological Disasters around Pipelines in Mountainous Areas. *Sci. Total Environ.* **2023**, *889*, 164334. [CrossRef] [PubMed]
50. Yan, Y.; Zhuang, Q.; Zan, C.; Ren, J.; Yang, L.; Wen, Y.; Zeng, S.; Zhang, Q.; Kong, L. Using the Google Earth Engine to Rapidly Monitor Impacts of Geohazards on Ecological Quality in Highly Susceptible Areas. *Ecol. Indic.* **2021**, *132*, 108258. [CrossRef]
51. Li, Y.; Lei, Y.; Chen, B.; Chen, J. Evaluation of Geological Hazard Susceptibility Based on the Multi-Kernel Density Information Method. *Sci. Rep.* **2025**, *15*, 7892. [CrossRef] [PubMed]
52. Yu, J.; Hu, W.; Hou, L. Towards More Resilient Cities-Analyzing the Impact of New-Type Urbanization on Urban Resilience: Considering Spatial Spillover Boundaries. *Sustain. Cities Soc.* **2024**, *114*, 105735. [CrossRef]
53. Huang, J.; Wen, H.; Li, Z.; Zhang, Y. Landslide-Oriented Disaster Resilience Evaluation in Mountainous Cities: A Case Study in Chongqing, China. *Resilient Cities Struct.* **2024**, *3*, 34–51. [CrossRef]

Disclaimer/Publisher's Note: The statements, opinions and data contained in all publications are solely those of the individual author(s) and contributor(s) and not of MDPI and/or the editor(s). MDPI and/or the editor(s) disclaim responsibility for any injury to people or property resulting from any ideas, methods, instructions or products referred to in the content.